Shock-Wave Reflection from a Turbulent Boundary Layer with Mass Bleed

WILLIAM R. SEEBAUGH* AND GERALD C. PAYNTER†
The Boeing Company, Seattle, Wash.

AND

MORRIS E. CHILDS‡
University of Washington, Seattle, Wash.

Methods for calculating the changes in turbulent boundary-layer characteristics across an oblique shock reflection based on integral flow models are developed for two-dimensional and axially symmetric flows with solid boundaries and mass bleed through porous walls, slots, or scoops. For each model, a control surface is assumed about the region of interaction; the velocity profiles upstream and downstream of the interaction are assumed to be power laws, and the integral continuity and momentum equations are written for the control volume. For a given mass-bleed configuration, specification of the upstream conditions and the bleed rate permits solution for the downstream boundary-layer thickness and velocity-profile exponent. Numerical results are presented for a range of upstream Mach numbers, mass-bleed rates, and incident-shock strengths. Comparison with data for two-dimensional shock reflections with zero bleed indicates that the analysis yields the correct trends.

Nomenclature

C	= Crocco number = $u/u_{\max}$
K	= function of C and N_i
M	= Mach number
$\dot{m}_B$	= bleed rate
$\dot{m}_B/\dot{m}_{BL}$	= ratio of bleed rate to upstream boundary-layer flow rate
N	= power-law exponent
p	= static pressure
R, R''	= radii defined in Fig. 2
T	= temperature
u	= x component of velocity
u^*	= u/u_e
(x,r)	= cylindrical coordinates
(x,y), (x',y'), (x'',y'')	= rectangular Cartesian coordinates
(X,Y), (X',Y')	= transformed coordinates
α	= incident-shock-wave flow-deflection angle
γ	= ratio of specific heats
δ	= boundary-layer thickness
δ^*	= displacement thickness
δ_c	= cone half-angle
Δ	= transformed boundary-layer thickness
θ	= momentum thickness
ρ	= density
ρ^*	= ρ/ρ_e

Subscripts

c	= compressible
e	= local external flow
i	= incompressible
s	= scoop
t	= total or stagnation
u	= streamline associated with bleed flow at upstream station
1,2,3	= flow regions and stations defined in diagrams of flow models

Presented as Paper 68-110 at the AIAA 6th Aerospace Sciences Meeting, New York, January 22–24, 1968; submitted January 18, 1968; revision received June 3, 1968.

* Research Specialist, Missile and Information Systems Division; formerly Predoctoral Research Associate, University of Washington, Seattle, Wash. Associate Member AIAA.

† Research Specialist, Commercial Airplane Division. Member AIAA.

‡ Professor, Department of Mechanical Engineering. Member AIAA.

1. Introduction

THE reflection of an oblique shock wave from a turbulent boundary layer is a flow phenomenon that occurs in inlets with supersonic internal compression. The interaction associated with the shock reflection is known to induce changes in the thickness of the boundary layer and in the shape of the velocity profile. If the pressure rise across the interaction is of sufficient strength, the resulting changes in boundary-layer characteristics may adversely affect inlet performance, particularly if flow separation occurs. The boundary layer downstream of the interaction may thicken rapidly and may be more susceptible to separation when subjected to further adverse pressure gradients. If not controlled, these effects may result in lower inlet-total-pressure recovery and increased flow distortion.

A very common method of boundary-layer control in inlets involves bleeding part of the boundary layer through porous walls, slots, or scoops. Removal of a portion of the boundary layer increases the pressure rise that the boundary layer can withstand without separating, reduces the thickness of the layer, and changes the shape of the velocity profile.

It is desirable to include the effects of a shock reflection on the boundary-layer profile shape and thickness in the calculation of the inlet flowfield. The objective of the present study was the development of methods for calculating the changes in turbulent boundary-layer characteristics across the reflection of an oblique shock with mass bleed through the region of interaction for both two-dimensional and axially symmetric flows. Results from these analyses, including changes in boundary-layer thickness, velocity-profile shape, and integral-thickness parameters, are presented for a range of Mach numbers, boundary-layer bleed rates, and shock strengths. Comparison with experiment is made where data are available.

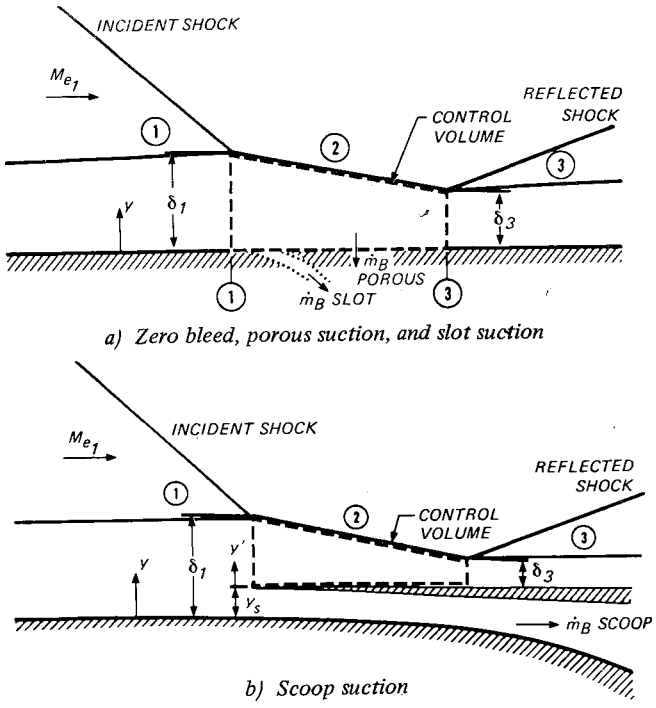

Fig. 1 Two-dimensional flow models.

1.1 Two-Dimensional Flow

In the reflection of an oblique shock from a turbulent boundary layer, the presence of subsonic flow near the wall permits the static-pressure rise across the shock reflection to propagate forward of the point of inviscid intersection of the incident shock with the wall, generating a band of compression wavelets that coalesce into the reflected shock. The reflected shock thus originates somewhat upstream of the point of inviscid intersection of the incident shock with the wall, and the incident and reflected shocks intersect at some point within the boundary layer. The distance from the wall to the point of intersection increases with increasing incident-shock strength.

The over-all effect of the shock reflection on the boundary layer is to make the velocity profile less full and to change its thickness. The flow external to the boundary layer approximates that predicted by oblique shock-wave theory. The external flow downstream of the reflected shock is nearly uniform and undergoes only small changes in flow properties as a result of the growth of the downstream boundary layer.

With consideration given to the previous description of the flow through the region of interest and methods of analysis proposed by Reshotko and Tucker,[1] Benson and Maslowe,[2] and Kutschenreuter et al.,[3] the following assumptions were made in the formulation of the two-dimensional flow models illustrated in Fig. 1. 1) The static-pressure distribution through the region of interaction external to the boundary layer is known from oblique shock theory. 2) The boundary-layer thickness and velocity-profile shape upstream of the interaction region are known. 3) The entrainment of mass from the external flow into the boundary layer through the region of interaction is negligible. 4) Frictional forces are negligible through the region of interaction. 5) The flow is isoenergetic. 6) The static-pressure rise starts downstream of the point where the incident shock enters the boundary layer and the reflected shock emerges downstream of the region of the static-pressure rise. 7) The velocity profile is adequately represented by a power law of the form

$$u^* = (y/\delta)^{1/N_c} \tag{1}$$

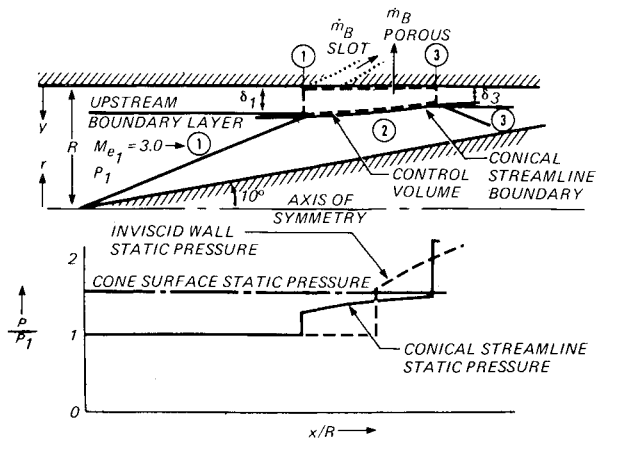

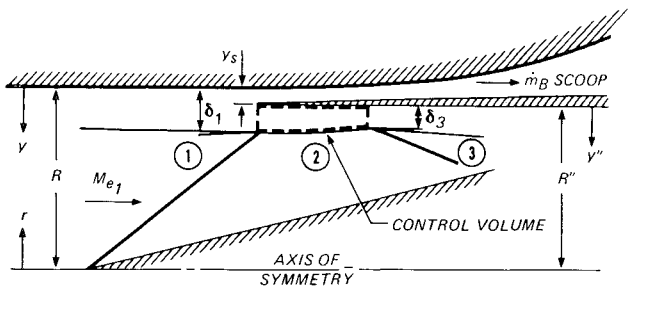

Fig. 2 Axially symmetric flow models.

1.2 Axially Symmetric Flow

The flow models for the axially symmetric shock-wave/boundary-layer interaction are illustrated in Fig. 2. A shock wave, such as that generated by a cone at zero angle of attack, reflects from the turbulent boundary layer that is developing on the inner surface of a duct. An inviscid analysis provides the theoretical point of shock impingement on the wall of the duct and the ideal static-pressure distribution at the wall. A continuous compression occurs downstream of the reflected shock in axially symmetric flow, whereas the pressure in this region remains constant for the corresponding two-dimensional case. The strength of the reflected shock increases with distance from the point of reflection. The pressure distributions illustrated in Fig. 2 are for a conical incident shock in uniform flow; however, the results of inviscid-flow calculations for inlets with supersonic internal compression show similar characteristics for shock reflections from both cowl and centerbody surfaces.

The flow external to the boundary layer is assumed to be determined from inviscid-flow theory. Since the static pressure in the region between the incident and reflected shock is not constant for conical and other axially symmetric flows, the external-flow streamlines are curved. With this modifi-

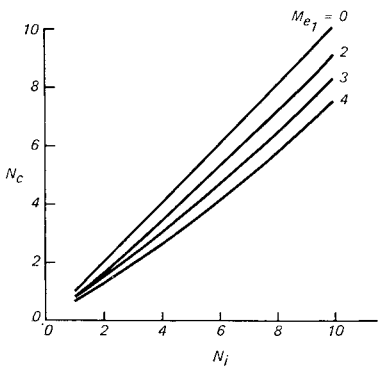

Fig. 3 Relation between N_c and N_i for the Dorodnitsyn-Howarth transformation.

cation, the assumptions stated for two-dimensional flow also apply to the axially symmetric case.

2. Analysis

2.1 Two-Dimensional Flow

The general method of analysis for the boundary-layer thickness and velocity-profile exponent downstream of the region of interaction is as follows. The equations of continuity and momentum are written for the assumed control volume, and the Dorodnitsyn-Howarth transformation[4] is applied. The transformed equations are solved for the transformed boundary-layer thickness and velocity-profile exponent. Application of the inverse transformation to these quantities yields the compressible boundary-layer thickness and velocity-profile exponent downstream of the reflected shock. This method of analysis is applied to control volumes for several mass-bleed configurations. The bleed models considered are porous-wall suction, in which no x-momentum flux is associated with the bleed flow, slot suction, in which an x-momentum flux term is associated with the bleed flow, and scoop suction.

Porous-wall suction

For the control volume shown in Fig. 1a, the continuity equation may be written

$$\left(1 - \frac{\dot{m}_B}{\dot{m}_{BL}}\right) \rho_{e_1} u_{e_1} \int_0^{\delta_1} \rho^* u^* dy|_1 = \rho_{e_3} u_{e_3} \int_0^{\delta_3} \rho^* u^* dy|_3 \quad (2)$$

and the momentum equation may be written

$$p_1\delta_1 - p_3\delta_3 - p_2(\delta_3 - \delta_1) = \rho_{e_3} u_{e_3}^2 \int_0^{\delta_3} \rho^* u^{*2} dy|_3 - \rho_{e_1} u_{e_1}^2 \int_0^{\delta_1} \rho^* u^{*2} dy|_1 \quad (3)$$

If the Dorodnitsyn-Howarth transformation[4] is applied,

$$X = X(x,y) = x \qquad Y = Y(x,y) = \int_0^y \rho^* dy \quad (4)$$

where the velocity profile in the transformed coordinates has the form

$$u^* = (Y/\Delta)^{1/N_i}$$

the continuity equation becomes

$$\frac{\Delta_1}{\Delta_3} = \frac{p_3 M_{e_3}(T_{e_1}/T_t)^{1/2}(1 + N_{i_1})N_{i_3}}{p_1 M_{e_1}(T_{e_3}/T)^{1/2} N_{i_1}(1 + N_{i_3})(1 - \dot{m}_B/\dot{m}_{BL})} \quad (5)$$

and the momentum equation may be written in the form

$$\frac{\Delta_1}{\Delta_3} = \frac{K_3(p_3/p_1 - p_2/p_1) + (p_3/p_1)\gamma M_{e_3}^2 N_{i_3}/(2 + N_{i_3})}{K_1(1 - p_2/p_1) + \gamma M_{e_1}^2 N_{i_1}/(2 + N_{i_1})} \quad (6)$$

where

$$K = [1/(1 - C_e^2)][1 - C_e^2 N_i/(2 + N_i)]$$

If the right-hand sides of the transformed continuity and momentum equations are equated, the resulting expression is a quadratic in terms of N_{i_3}. The solution for N_{i_3} can be substituted into Eq. (5) or Eq. (6) to obtain Δ_1/Δ_3. The invariance of the stream function with respect to coordinate transformation gives the relation between N_{i_3} and N_{c_3} (Fig. 3). The expression for δ_1/δ_3 in terms of Δ_1/Δ_3 is, from the transformation,

$$\delta_1/\delta_3 = \Delta_1 K_1/\Delta_3 K_3 \quad (7)$$

Slot-wall suction

The slot geometry, considered for the slot-wall suction model, is shown by the dashed lines in Fig. 1a. The control volume is the same as for the porous wall. The continuity equation, Eq. (2), for the porous wall also applies to the slot-wall configuration. The x-momentum flux across the control surface through the slot is set equal to the x-momentum associated with the flow in a streamtube crossing station 1 of the control volume (Fig. 1a). At station 1, this streamtube, with mass flux equal to the bleed flow rate, is bounded by the wall and the appropriate streamline in the upstream boundary layer. The momentum equation may then be written, and transformed, as for the porous-wall model,

$$\frac{\Delta_1}{\Delta_3} = \frac{(p_3/p_1 - p_2/p_1)K_3 + [(p_3/p_1)\gamma M_{e_3}^2 N_{i_3}]/(2 + N_{i_3})}{(1 - p_2/p_1)K_1 + \gamma M_{e_1}^2 N_{i_1}/(2 + N_{i_1}) \times [1 - (\dot{m}_B/\dot{m}_{BL})^{(2+N_{i_1})/(1+N_{i_1})}]} \quad (8)$$

If the right-hand sides of the transformed-continuity and momentum equations are equated, δ_1/δ_3 and N_{c_3} may be obtained as for the porous-wall case.

Scoop suction

The control volume for scoop suction (Fig. 1b) is somewhat different from that of the previous cases. The continuity equation may be written in the form

$$\left(1 - \frac{\dot{m}_B}{\dot{m}_{BL}}\right) \rho_{e_1} u_{e_1} \int_0^{\delta_1} \rho^* u^* dy|_1 = \rho_{e_3} u_{e_3} \int_0^{\delta_3} \rho^* u^* dy'|_3 \quad (9)$$

Applying the Dorodnitsyn-Howarth transformation and rearranging,

$$\frac{\Delta_1}{\Delta_3} = \frac{p_3 M_{e_3}(T_{e_1}/T_t)^{1/2}(1 + N_{i_1})N_{i_3}}{p_1 M_{e_1}(T_{e_3}/T_t)^{1/2}(1 + N_{i_3})N_{i_1}(1 - \dot{m}_B/\dot{m}_{BL})} \quad (10)$$

The momentum equation may be stated as

$$p_1(\delta - y_s) - p_2(\delta_1 - \delta_3 - y_s) - p_3\delta_3 = \int_0^{\delta_3} \rho u^2 dy'|_3 - \int_{y_s}^{\delta_1} \rho u^2 dy|_1 \quad (11)$$

Again applying the Dorodnitsyn-Howarth transformation and rearranging,

$$\frac{\Delta_1}{\Delta_3} = \frac{K_3(p_3/p_1) - (p_2/p_1) + (p_3/p_1)\gamma M_{e_3}^2 N_{i_3}/(2 + N_{i_3})}{K_1(1 - p_2/p_1) + K_{s_1}(p_2/p_1 - 1) + \gamma M_{e_1}^2 N_{i_1}/(2 + N_{i_1})[1 - (Y_s/\Delta_1)^{(2+N_{i_1})/N_{i_1}}]} \quad (12)$$

where

$$K_{s_1} = \frac{1}{1 - C_{e_1}^2}\left[\frac{Y_s}{\Delta_1} - \frac{C_{e_1}^2 N_{i_1}}{2 + N_{i_1}}\left(\frac{Y_s}{\Delta_1}\right)^{(2+N_{i_1})/N_{i_1}}\right]$$

and

$$Y_s/\Delta_1 = \dot{m}_B/\dot{m}_{BL}{}^{N_{i_1}/(1+N_{i_1})}$$

By equating the right-hand side of the transformed continuity and momentum equations, δ_1/δ_3 and N_{c_3} may be obtained as in the porous-wall and slot-suction cases.

Direct solution of the continuity and momentum equations

The continuity and momentum equations may also be solved directly for δ_1/δ_3 and N_{c_3}, using a numerical integration procedure to evaluate the mass and momentum-flux integrals. The direct and the transformation solutions were compared for a number of specific cases and the results obtained were found to be in good agreement. Because of the simplicity of solution and the compatibility of the transformation analysis with integral boundary-layer methods such as that of Sasman and Cresci,[5] the transformation method was used for the two-dimensional flow solutions of the present study.

2.2 Axially Symmetric Flow

For the two-dimensional flow models, the external static pressures and Mach numbers are known from the oblique

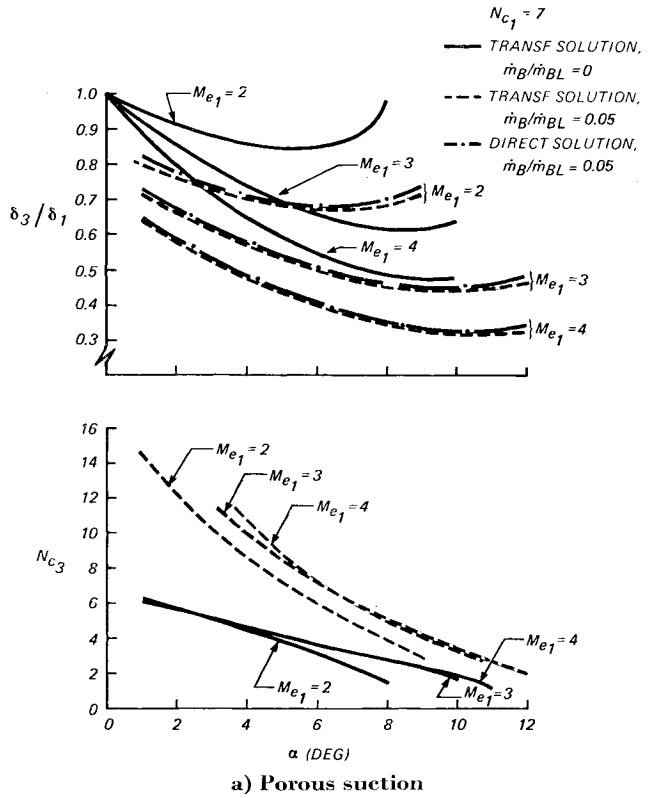

a) Porous suction

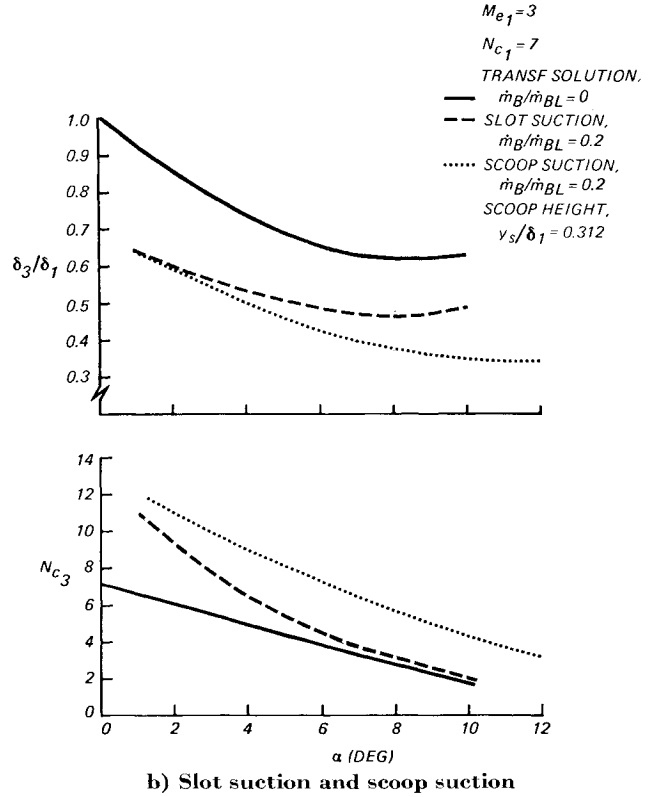

b) Slot suction and scoop suction

Fig. 4 Boundary-layer thickness ratios and downstream power-law exponents for two-dimensional flow.

shock-wave equations and are independent of the downstream boundary-layer thickness. Since the external-flow streamlines in the region between the incident and reflected shocks are curved for axially symmetric flow, the properties downstream of the reflected shock are initially unknown. The boundary-layer integral equations must be solved simultaneously with a relationship for the static pressure, Mach number, and flow angle along the external-flow streamline at the edge of the boundary layer. The external-flow properties downstream of the reflected shock are obtained using the oblique shock-wave equations, assuming that the downstream flow is parallel to the wall.

The integral continuity and momentum equations for axially symmetric flow are similar to those obtained for the two-dimensional case. All integrals are taken over the annular region from $r = R - \delta$ to $r = R$ (Fig. 2). The cross-sectional geometry of the interaction region is similar to that for two-dimensional flow except that the boundary streamline of region 2 is generally curved.

Porous-wall suction

The continuity equation for axially symmetric porous-wall suction (Fig. 2a) may be written in the form

$$2\pi\left(1 - \frac{\dot{m}_B}{\dot{m}_{BL}}\right)\rho_{e_1}u_{e_1}\int_{R-\delta_1}^{R}\rho^*u^*rdr|_1 = 2\pi\rho_{e_3}u_{e_3}\int_{R-\delta_3}^{R}\rho^*u^*rdr|_3 \quad (13)$$

The corresponding momentum equation may be expressed in the form

$$\pi(2R\delta_1 - \delta_1^2)p_1 - \pi(2R\delta_3 - \delta_3^2)p_3 - 2\pi\int_{R-\delta_1}^{R-\delta_3} p_{2_e}rdr = 2\pi\rho_{e_3}u_{e_3}^2\int_{R-\delta_3}^{R}\rho^*u^{*2}rdr|_3 - 2\pi\rho_{e_1}u_{e_1}^2\int_{R-\delta_1}^{R}\rho^*u^{*2}rdr|_1 \quad (14)$$

where p_{2_e} is the variable pressure along the boundary streamline.

The necessary information for the external-flow streamline may be determined by method-of-characteristics calculations for the flows encountered in supersonic inlets. For the results that follow, the flow model illustrated in Fig. 2a was employed and the inviscid-streamline data were calculated using conical-flow theory. The integral term

$$2\pi\int_{R-\delta_1}^{R-\delta_3} p_{2_e}rdr$$

was evaluated by solving the differential equations numerically, tracing a streamline from the intersection of the incident shock and the edge of the approaching boundary layer, and integrating along the resulting streamline. Since the integrations necessary in the conical-flow calculation require the use of a digital computer, it was considered more convenient to program the entire axially symmetric analysis for the computer and use the direct-solution procedure instead of applying the Dorodnitsyn-Howarth transformation.

Slot-wall suction

The slot geometry and the control volume for slot-wall suction are illustrated in Fig. 2a. The continuity equation for the porous wall, Eq. (13), also applies to the slot-suction model. The momentum equation, written in the form of Eq. (14), becomes

$$\pi(2R\delta_1 - \delta_1^2)p_1 - \pi(2R\delta_3 - \delta_3^2)p_3 - 2\pi\int_{R-\delta_1}^{R-\delta_3} p_{2_e}rdr = 2\pi\rho_{e_3}u_{e_3}^2\int_{R-\delta_3}^{R}\rho^*u^{*2}rdr|_3 - 2\pi\rho_{e_1}u_{e_1}^2\int_{R-\delta_1}^{R-y_u}\rho^*u^{*2}rdr|_1 \quad (15)$$

where the x momentum transferred across the control surface through the slot is set equal to the x momentum of the bleed flow at the upstream station. The distance y_u is given by

$$\dot{m}_B = \int_{R-y_u}^{R} 2\pi\rho urdr|_1 \quad (16)$$

and represents the distance from the wall to the stream surface that encloses the mass removed through the slot. The solution of Eqs. (13, 15, and 16) is obtained by the procedure described previously for the porous-wall model.

Scoop suction

The control volume used for axially symmetric scoop suction is illustrated in Fig. 2b. As shown, the duct radius downstream of the interaction is reduced by an amount equal to the scoop height. Accounting for this change in duct radius, the continuity equation may be stated in the form

$$2\pi\rho_{e_1}u_{e_1}\int_{R-\delta_1}^{R-y_s}\rho^*u^*rdr|_1 = 2\pi\rho_{e_3}u_{e_3}\int_{R''-\delta_3}^{R''}\rho^*u^*rdr|_3 \quad (17)$$

The corresponding momentum equation is then

$$\pi(2R\delta_1 - \delta_1^2)p_1 - \pi(2Ry_s - y_s^2)p_1 - \pi(2R''\delta_3 - \delta_3^2)p_3 - \int_{R-\delta_1}^{R''-\delta_3}2\pi p_{2_e}rdr = 2\pi\rho_{e_3}u_{e_3}^2\int_{R''-\delta_3}^{R''}\rho^*u^{*2}rdr|_3 - 2\pi\rho_{e_1}u_{e_1}^2\int_{R-\delta_1}^{R-y_s}\rho^*u^{*2}rdr|_1 \quad (18)$$

Equations (17) and (18) are solved by the procedure outlined previously for the porous-wall and slot-suction cases.

3. Results and Discussion

Predictions of δ_3/δ_1 for zero bleed flow and a porous-suction flow rate of 0.05 times the upstream boundary-layer mass flow may be compared in Fig. 4a. The compressible power-law exponent is 7, which is representative of typical flat-plate turbulent boundary-layer velocity profiles for the Mach number range of 2 to 4. The results for δ_3/δ_1 with zero bleed exhibit the correct dependence on incident-shock strength,[6] that is, decreasing over a range of incident-shock-wave flow-deflection angles, reaching a minimum, and then increasing for higher strength shocks. The incident-shock-wave deflection angles of interest in inlet flows are generally lower than those corresponding to the minimum values of δ_3/δ_1 because of the necessity for high pressure recovery in the inviscid flow.

Results of the transformation and direct solutions may also be compared in Fig. 4a. The agreement is excellent for intermediate-strength shocks, and differences are within 7% over the entire range of variables. Subsequent results shown for two-dimensional flow were obtained by the transformation solution procedure.

The compressible power-law exponents downstream of the interaction for zero and 5% porous-suction flow rates are also given in Fig. 4a for $N_{c_1} = 7$. These results indicate that the use of bleed increases N_{c_3} at a given shock strength, and that an increase in shock strength causes a reduction in N_{c_3} for all cases. The dependence of the downstream power-law exponent on the upstream Mach number decreases with increasing M_{e_1}.

A bleed-flow rate of 5% of the initial mass flow is considered to be representative of the maximum rate that is consistent with the porous-wall suction model. Higher rates would require large bleed holes or an extended porous region upstream of the interaction. With large bleed holes, the slot-suction model may provide a closer approximation to the actual flow configuration, since the x momentum associated with bleed through large holes could be significant. For a configuration with an extended porous region upstream of the interaction, modifications to the flow models of the present study to allow for mass entrainment and skin-friction effects would be necessary.

The effects of slot and scoop suction on δ_3/δ_1 and N_{c_3} are shown in Fig. 4b for the upstream conditions $M_{e_1} = 3$ and $N_{c_1} = 7$. By comparing slot-suction results at several bleed flow rates with the predictions shown for porous suction, it was determined that a bleed rate of 20% of the upstream boundary layer was required to obtain comparable boundary-layer thickness ratios. This bleed rate is believed to be more representative of requirements for inlet flows than lower flow rates, and the results presented are based on 20% slot suction. The bleed rate for scoop suction was selected to allow a direct comparison of results with those of the slot-suction analysis.

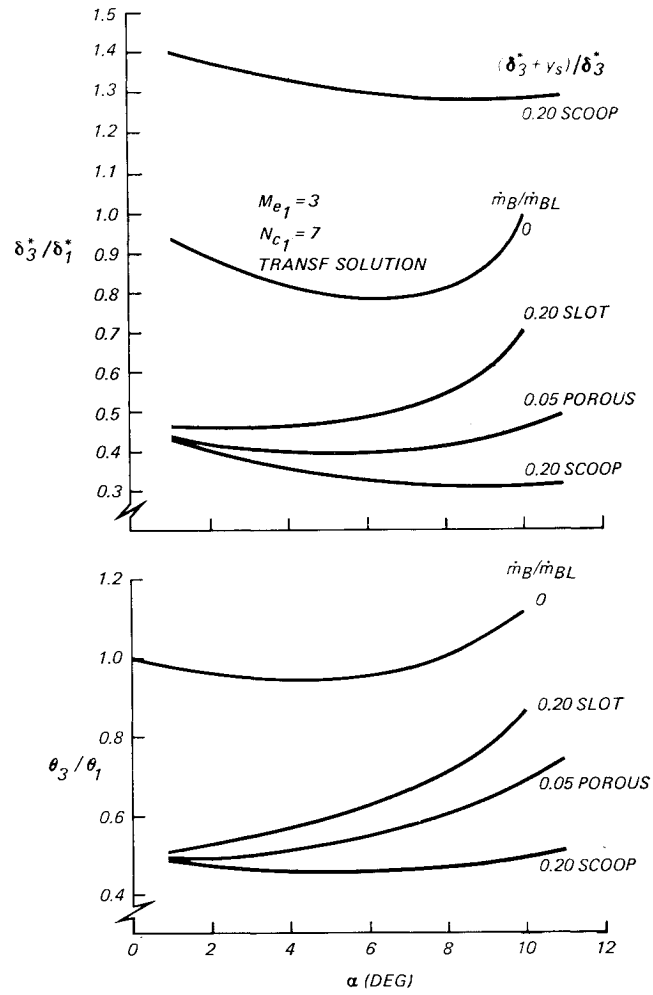

Fig. 5 Displacement momentum thickness ratios for all suction configurations, two-dimensional flow.

Ratios of displacement and momentum thicknesses across the shock reflection are given in Fig. 5 for the upstream conditions $M_{e_1} = 3$ and $N_{c_1} = 7$. The minimum values of the integral thickness ratios occur at incident-shock-wave flow-deflection angles that are lower than those for the minima of δ_3/δ_1. With no mass bleed, the integral-thickness ratios are always greater than the corresponding values of δ_3/δ_1. The introduction of suction results in lower integral-thickness ratios at lower shock strengths and in lower boundary-layer thickness ratios at higher incident-shock-wave flow-deflection angles. The total effective displacement of the external flow downstream of the interaction for scoop suction, represented by $(\delta_3^* + y_s)/\delta_1^*$, is also shown in Fig. 5.

The influence of the ratio of upstream boundary-layer thickness to duct radius with zero suction is shown in Fig. 6a for the upstream conditions $M_{e_1} = 3$ and $N_{c_1} = 7$. The combined effects of the varying over-all pressure ratio p_3/p_1 and the change in flow area per unit radius with distance from the wall cause significant changes in δ_3/δ_1 and in N_{c_3} relative to the corresponding two-dimensional flows. As δ_1/R is increased, the minimum value of δ_3/δ_1 decreases and the minima occur at successively lower shock strengths. The effect of increasing δ_1/R is similar to that obtained by increasing the shock strength for two-dimensional flow, and is primarily due to the increase in p_3/p_1 resulting from the compression along the conical streamline at the edge of the boundary layer and the stronger reflected shock.

Results for the three types of boundary-layer suction are presented in Fig. 6b for $\delta_1/R = 0.1$. The dependence of

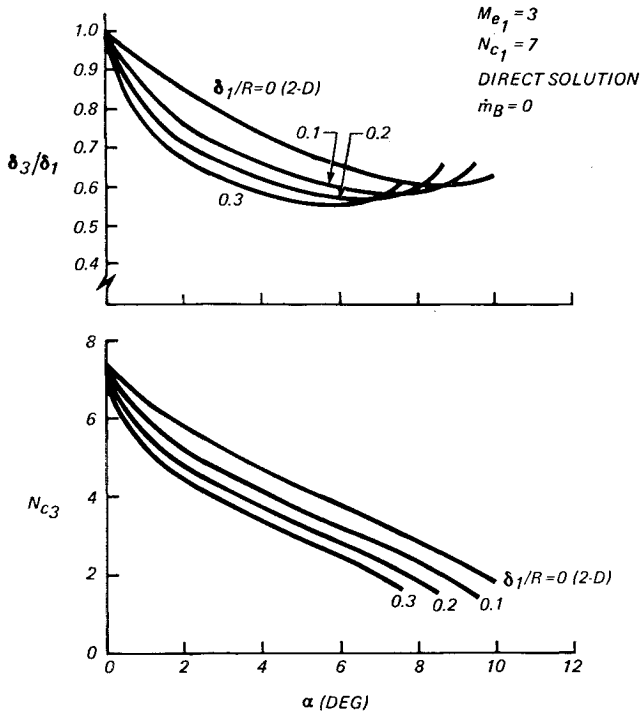

a) For zero bleed, two-dimensional and axially symmetric flows

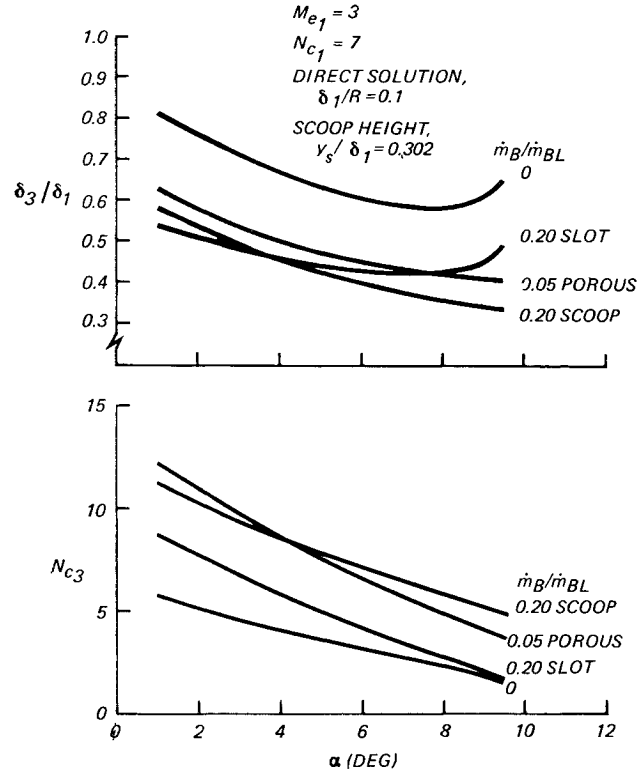

b) For all suction configurations, axially symmetric flow

Fig. 6 Boundary-layer thickness ratios and downstream power-law exponents.

δ_3/δ_1 on shock strength is similar to that for two-dimensional flow. The introduction of suction results in an increase in N_{c_3} for all axially symmetric bleed configurations.

4. Comparison with Data

Detailed experimental information on the effects of mass bleed on the changes in boundary-layer thickness and velocity-profile parameter across a shock reflection is not currently available for any of the suction models discussed in this paper.

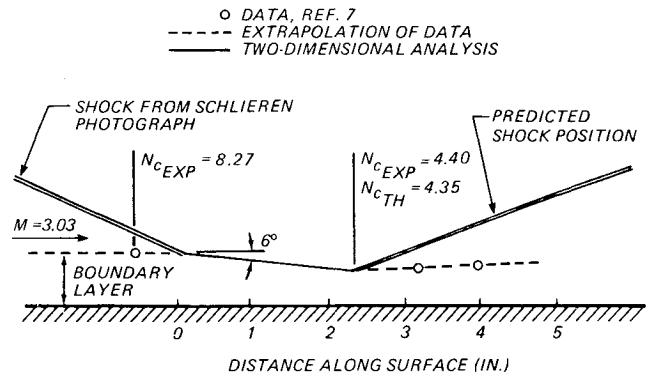

Fig. 7 Predicted and measured results for shock interaction with zero bleed.

The results of calculations for a two-dimensional shock reflection without mass bleed are compared with experimental data reported by Pinckney[7] in Fig. 7. The boundary-layer characteristics downstream of the shock reflection were given for two stations, as shown. The theoretical predictions apply to a station upstream of the nearest location at which boundary-layer data were acquired. When a linear extrapolation of the experimental values of δ_3/δ_1 and N_{c_3} to the correct station was made, the predicted results for δ_3/δ_1 and N_{c_3} were within 1% of the experimental data.

The possibility of influences of mass entrainment and the attendant momentum transfer on the results for two-dimensional flow without bleed were examined for the case shown in Fig. 7. From the experimental results reported in Ref. 7, an increase in boundary-layer mass flow equal to about 4% of the upstream value was obtained. A new flow model with mass addition and momentum transfer, assumed to occur across the upper control surface (Fig. 1), was postulated. Calculations for the upstream data corresponding to Fig. 7 with 4% mass addition indicated that δ_3/δ_1 increased by about 2% and N_{c_3} increased by about 6%. It was concluded that changes of such magnitude did not justify the additional assumptions or the introduction of empirical correlations that would be necessary to include the effects of entrainment from the external flow.

5. Conclusions

The results of the analytical methods outlined in this paper have been compared with available data and are believed to exhibit sufficiently close agreement with experiment to substantiate the assumptions of the flow models. The important results of the analysis and data comparisons are now summarized.

1) The axially symmetric flow analysis should be used for flow in round ducts when the ratio of upstream boundary-layer height-to-duct radius is greater than about 0.1. 2) The introduction of boundary-layer suction reduces δ_3/δ_1 and increases the power-law exponent relative to the values obtained without bleed for all suction models. 3) The transformation solution could be combined with a compressible boundary-layer method to provide complete predictions of boundary-layer properties for the supersonic diffuser of an internal-compression inlet. 4) The methods of analysis may be adapted to nonisoenergetic-flow cases by relating velocity and total temperature profiles, as, for example, through the use of the Crocco relation.

References

[1] Reshotko, E. and Tucker, M., "Effect of a Discontinuity on

Turbulent Boundary-Layer-Thickness Parameters with Application to Shock-Induced Separation," TN 3454, May 1955, NACA.

[2] Benson, J. L. and Maslowe, S. A., "Bluntness and Boundary Layer Displacement Effects on Hypersonic Inlet Flow Fields," Paper 65-617, June 1965, AIAA; also *Journal of Spacecraft and Rockets*, Vol. 3, No. 9, Sept. 1966, pp. 1394–1401.

[3] Kutschenreuter, P. A., Brown, D. L., and Hoelmer, W., "Investigation of Hypersonic Inlet Shock-Wave Boundary Layer Interaction," TR-65-36, Part II, April 1966, Air Force Flight Dynamics Lab.

[4] Stewartson, K., *The Theory of Laminar Boundary Layers in Compressible Fluids*, Oxford Mathematical Monograph, Oxford University Press, 1962.

[5] Sasman, P. K. and Cresci, R. J., "Compressible Turbulent Boundary Layer with Pressure Gradient and Heat Transfer," *AIAA Journal*, Vol. 4, No. 1, Jan. 1966, pp. 19–25.

[6] Pinckney, S. Z., "Semiempirical Method for Predicting Effects of Incident-Reflecting Shocks on the Turbulent Boundary Layer," TN D-3029, Oct. 1965, NASA.

[7] Pinckney, S. Z., "Data on Effects of Incident-Reflecting Shocks on the Turbulent Boundary Layer," TM X-1221, March 1966, NASA.

SEPT.-OCT. 1968 J. AIRCRAFT VOL. 5, NO. 5

Powerplant Aspects of High-Speed, Inter-City VTOL Aircraft

D. J. PICKERELL* AND R. A. CRESSWELL†
Rolls-Royce Ltd., Derby, England

This paper reviews the problems associated with installing an advanced self-contained lift fan engine in wing pods for a high-speed, inter-city civil VTOL aircraft. It is shown that community noise levels can be approached which will permit city-center aircraft operation. The advantages of using multiple self-contained lift fans are discussed together with general installation problems such as the design of low noise level air intake systems. Methods of providing aircraft control during transition and engine thrust deflection for acceleration are examined. It is concluded that, with the latest technology, podded installations of low noise level self-contained lift fans can be designed within the same installed volume as an equivalent RB 162 lift jet installation of the type now flying in the Dornier Do 31 military VTOL transport aircraft.

1. Introduction

Civil VTOL Field

THE rapid growth of conventional air transportation and increasing surface traffic congestion is providing a strong incentive to find a solution to the problem of civil VTOL operation. Of existing VTOL aircraft, the high subsonic cruising speed direct jet lift approach, although becoming accepted for military applications, is too noisy for city-center operation. The helicopter, although potentially quiet enough, suffers from severe speed and endurance problems.

A wide range of aircraft types, from compound helicopters through tilt wing and tilt propeller aircraft to fan lift aircraft, is currently being investigated. Except for very short haul duty, the emphasis is upon a reasonably high cruise speed to minimize journey time and to improve productivity. The combination of low noise level and high cruise speed potential, together with the engine-out safety requirements necessary for civil operation, can be met with the self-contained lift-fan concept. One possible evolutionary route from the German Dornier Do 31-1, the world's first military jet lift VTOL transport aircraft, to a high-speed, inter-city VTOL civil aircraft with pods of self-contained lift-fan engines is illustrated in Fig. 1.

Presented as Paper 67-745 at the AIAA/RAeS/CASI 10th Anglo-American Aeronautical Conference, Los Angeles, Calif., October 18–20, 1967; submitted November 17, 1967; revision received April 15, 1968. The authors wish to thank the directors of Rolls-Royce Ltd. for permission to publish this paper and the various specialist departments within the company for their valuable help. The authors are also indebted to both Dornier-Werke GmbH and Hawker Siddeley Aviation Ltd. for their pioneering work on jet lift VTOL transport aircraft.

* Assistant Chief of Preliminary Design.

† Head of Joint Installation Project Office.

Although it is possible that the ultimate inter-city VTOL civil aircraft using self-contained lift-fan engines will be one in which the powerplant and airframe are closely integrated, the separate lift pod concept remains a perfectly practical "first generation" solution. A conventional airframe can be employed, thus avoiding the combination of a new powerplant principle with a new airframe concept. With this arrangement it is relatively easy to take advantage of future developments in either lift- or propulsion-engine developments. If necessary, aircraft growth need not await lift-engine development, since the pod configuration allows the installation of extra lift engines with minimum airframe modifications.

Lift-Engine Development

The concept of VTOL using multiple single-purpose lift engines was originated by Dr. A. A. Griffith of Rolls-Royce, whose first paper on jet lift VTOL was presented to the Aeronautical Research Council in 1941. The RB 108 specialized lift jet first ran in 1955, to be followed by the RB 162 in 1961.

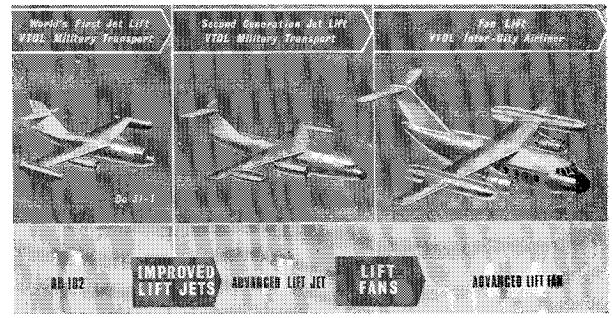

Fig. 1 Development of civil VTOL transport.